VHCF life of AM1 Ni-based single crystal superalloy after pre-deformation

Satoshi Utada, Luciana Maria Bortoluci Ormastroni, Jérémy Rame, Patrick Villechaise, Jonathan Cormier

VHCF life of AM1 Ni-based single crystal superalloy after pre-deformation

Satoshi Utada[1,2,*], Luciana Maria Bortoluci Ormastroni[1], Jérémy Rame[2],

Patrick Villechaise[1], Jonathan Cormier[1,*]

[1] Institut Pprime, UPR CNRS 3346, Physics and Mechanics of Materials Department, ISAE-ENSMA, BP 40109, 86961, Futuroscope-Chasseneuil Cedex, France
[2] Safran Aircraft Engines, Site de Villaroche, Rond-Point René Ravaud - Réau, 77550, Moissy-Cramayel, France
[*] corresponding authors: satoshi.utada@ensma.fr and jonathan.cormier@ensma.fr

Keywords: Ni-based single crystal superalloy; pre-deformation; very high cycle fatigue; rejuvenation

Abstract

VHCF properties of the Ni-based single crystal superalloy AM1 with pre-deformation have been investigated at 1000 °C. Pre-deformed material did not present life debit under fully reversed conditions (R = −1). Pre-deformation decreased VHCF lifetime under high mean stress conditions (R = 0.5) with a presence mode I surface crack initiation. The pre-deformed material has microstructure coarsened bands lying on the former {111} slip planes, facilitating microstructure shearing during VHCF at R = 0.5. Slip traces increased surface roughness, causing surface recrystallization and fatal surface crack. Rejuvenation heat treatment after pre-deformation can restore the microstructure and the fatigue life.

Highlights

- VHCF life of pre-deformed Ni-based single crystal superalloy at 1000 °C.
- Pre-deformation has no effect on the VHCF life at R = -1.
- Pre-deformation induces VHCF life debit at R = 0.5 and high mean stress.
- Rejuvenation heat treatment restores VHCF life.

1. Introduction

Very high cycle fatigue (VHCF) life of Ni-based single crystal (SX) superalloys in fully reversed stress condition (R= −1) is generally controlled by the size and position of the largest casting pores [1–5]. This mainly results from the stress concentration in pores' vicinity that activates γ/γ' microstructure shearing by slip bands [4]. In such conditions, a solidification pore (S-pore) in the interdendritic area becomes the main crack initiation site [6,7]. In a recent article by Cervellon et al., fatigue crack initiation mechanisms have been proposed for the VHCF regime (N_f >> 10^7) under fully reversed conditions at 1000 °C [4]. This study described that stress concentration near a large S-pore induces intense localized shearing of γ' precipitates activating recrystallization and interacting solute element concentration [4,8–10]. The local crack propagation threshold decreases as recrystallization proceeds. The crack propagation at the recrystallized area creates a “rough zone” at the fracture surface of a specimen failed by internal crack initiation [4].

On the other hand, the VHCF life of Ni-based SX superalloys at a positive ratio (R > 0) is affected by the γ/γ'

microstructure and the intrinsic creep strength [1,2,11]. Overaged and coarsened microstructures have lower creep durability and lower yield stress, especially at high applied stresses or higher strain rates [1,12]. Therefore, since the specimen is in tensile loading during all periods of positive ratio condition with a very high strain rate (in the order of 10^2 /s), creep damages such as microstructure coarsening and cracks initiating from creep voids also take place in this VHCF regime.

A plastic (pre-)deformation may occur during the processing (i.e. casting, heat treatments …) of airfoils made from Ni-based SX superalloys [8,13,14]. If such plastic deformation (PD) is introduced in a component after the solution heat treatment, three microstructural events take place during subsequent aging treatments [8,15]: 1) Faster γ/γ' microstructure evolution in the vicinity of the slip band compared to the area far from the slip band; 2) S-pore and homogenization-pore (H-pores [6,16]) growth assisted by enhanced γ/γ' microstructure evolution at the bands; 3) Dislocation climb favoring the nucleation of deformation pores (D-pores [17]) within the bands. Moreover, during creep loading at high temperature (≥ 950 °C), faster microstructure coarsening along the former slip band accelerates the creep damage accumulation at nucleated and enlarged pores, ultimately leading to a shorter creep life [8,15]. When creep testing at a lower temperature with higher applied stresses (e.g., 850 °C / 500 MPa), γ/γ' microstructure shearing from creep void was observed locally in the microstructure coarsened band [8,14]. Considering these microstructure evolutions and high-temperature behaviors of pre-deformed AM1 Ni-based SX superalloy, coarsened pores lying in the microstructure coarsened band with lower resistance to shearing may decrease the high-temperature fatigue life of the material.

Within this context, this study aims at investigating the influence of microstructural defects induced by prior plastic deformation on the VHCF lifetime of the AM1 SX superalloy. Another objective is to improve the understanding of fracture mechanisms in the VHCF regime at 1000 °C, both in fully reversed ($R = -1$) and with the application of a mean stress ($R = 0.5$). The experiments are achieved by a specifically-designed two-step machining procedure to obtain pre-deformed VHCF specimens. Because turbine blades may be pre-deformed during production [8,13–15], and since high cycle fatigue properties have been imposed as new turbine airfoil design criteria by the airworthiness authorities (FAA, EASA), evaluating fatigue properties of pre-deformed material is an essential matter. Rejuvenation heat treatment, which can restore microstructure and creep life after pre-deformation [14], is also tested in this study to evaluate its efficiency in restoring VHCF life.

2. Experimental procedures

Solution-treated SX bars (14 mm diameter) of the Ni-based superalloy AM1 (Ni-7.6Cr-6.7Co-5.6W-2Mo-8Ta-5.2Al-1.2Ti-0.05Hf, wt.%) used in this study are from the same casting batch as our previous study [15]. SX bars with excellent crystallographic orientation (longitudinal misorientation from the perfect <001> direction less than 2°) were chosen for this study. VHCF test specimens with pre-deformation were prepared by following steps including two-step machining: 1) Machining SX bars into tensile test specimen (geometry given in Figure 1(a)) with parallel gauge section (i.e. smooth gauge part); 2) Mechanical polishing of a gauge section using P4000 SiC abrasive paper to remove residual stresses inherited from machining; 3) Apply

tensile prior plastic deformation at room-temperature at a strain rate of 5.0×10^{-4} /s using an Instron 8562 electromechanical machine. Plastic strain of the pre-deformed specimen was controlled at ~ 0.8% using an extensometer; 4) Aging heat treatments consisting of standard first (at 1100 °C for 5 h, air quench) and second (at 870 °C for 16 h, air quench) stages in the air using a resistive furnace; 5) Second machining into hourglass-shaped VHCF specimen with the geometry given in Figure 1(b) [1]; 6) Surface polishing up to a mirror finish (1 µm diamond paste) to remove residual stresses and plastically deformed layer coming from machining and to minimize surface roughness. These steps are presented as a diagram in Figure 2.

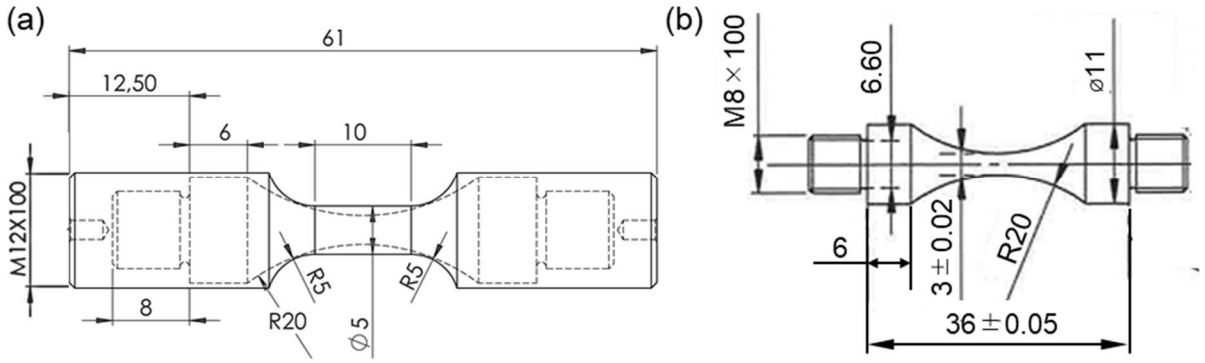

Figure 1. Geometries of cylindrical gauge specimens for tensile pre-deformation (a) and hourglass-shaped specimens for the VHCF test (b).

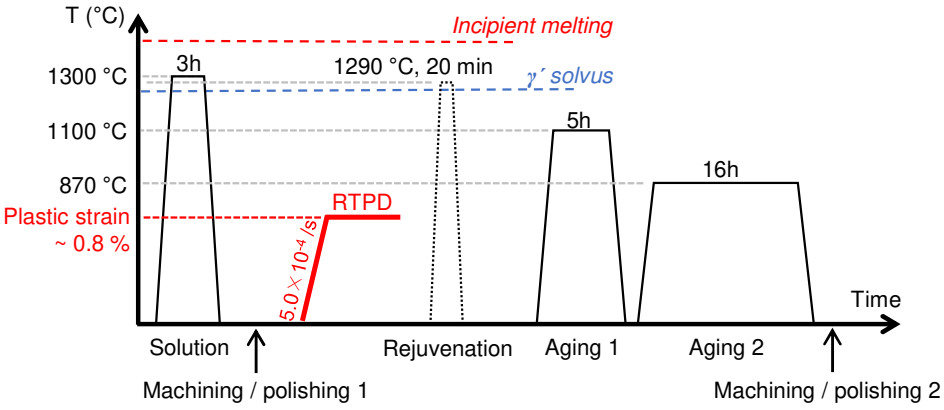

Figure 2. Material history diagram showing an order of machining/polishing, RTPD (room temperature plastic deformation), rejuvenation, and aging treatments.

The pre-deformed specimen is named “AM1-RTPD-HT1”, whereas reference material without PD is named “AM1-HT1”. The VHCF test using an ultrasonic fatigue machine requires a specimen with precise geometry to achieve resonance at ~20 kHz and 1000 °C. Therefore, VHCF specimens were machined from larger cylindrical specimens to introduce controlled pre-deformation strain in the central part of the VHCF specimen without changing the geometry. Rejuvenation treatment at 1290 °C for 20 min (air quench) was inserted between pre-deformation and aging treatments for microstructure restoration (this specimen is named “AM1-RTPD-Rejuv-HT1”). The rejuvenation treatment condition for pre-deformed AM1 was investigated and determined previously [14].

Initial microstructures of AM1-RTPD-HT1 and AM1-RTPD-Rejuv-HT1 are shown in Figure 2. Bands of coarsened γ′ precipitates were observed in AM1-RTPD-HT1 and they are called "microstructure coarsened bands" whereas they were absent in AM1-RTPD-Rejuv-HT1. Diameter of S-pores (black arrows in Figure 2) was measured using the surrounding diameter method [18] and it was 70 µm at maximum for both AM1-RTPD-HT1 and AM1-RTPD-Rejuv-HT1, a value equivalent to the one measured in AM1 SX superalloy tested in the previous study [2]. D-pores (white arrows in Figure 2(a)) were nucleated in AM1-RTPD-HT1 during aging treatments. Details of the microstructure coarsened bands and pores are available in previous studies from the authors [8,15]. In addition, AM1-RTPD-Rejuv-HT1 presented equivalent γ/γ′ microstructure to AM1-HT1 [14].

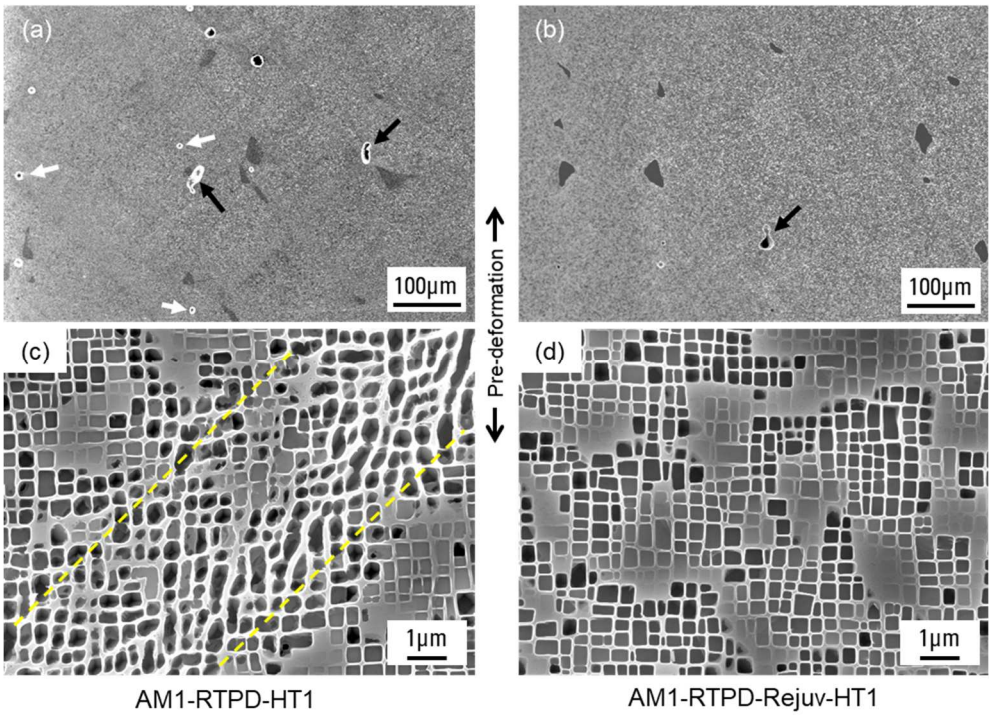

Figure 3. Initial microstructure of AM1-RTPD-HT1 (a, c) and AM1-RTPD-Rejuv-HT1 (b, d). Black and white arrows in lower magnification images (a, b) are pointing at S-pores and D-pores, respectively. Dotted lines in (c) are indicating the microstructure coarsened band.

All fatigue tests were performed at 1000 °C, 20 kHz, and $R = -1$ and 0.5 using an ultrasonic fatigue machine following the procedures described previously [1–4]. The VHCF specimen is designed specifically for the testing machine and its first tension/compression mode resonant frequency is 20 ± 0.5 kHz. Specimen center was heated by induction heating method and the temperature was measured and controlled using a dual-wavelength pyrometer, forming a closed-loop temperature controlling system. PID parameters of the induction heating device were adjusted so as to achieve an excellent temperature control at 1000 °C (+/- 2 °C) despite self-heating of the specimens that may occur at high alternating stresses (σ_a > 200 MPa) in the beginning of the tests. A piezoelectric transducer transformed a sinusoidal electrical signal into a longitudinal mechanical wave which was amplified by an ultrasonic horn. Tests at $R = -1$ were performed under strain-controlled mode. A constant mean load was applied using a pneumatic device for the tests at $R = 0.5$.

Fractographic and microstructural analyses of failed specimens were performed using an optical microscope and a

field emission gun scanning electron microscope (JEOL JSM-7000F). Longitudinal cross sections of AM1-RTPD-HT1 specimens after VHCF tests at 1000 °C, f = 20 kHz, R = −1, σ_a = 209 MPa and at 1000 °C, f = 20 kHz, R = 0.5, σ_{max} = 551 MPa were prepared for microstructure observations. A combination of mechanical polishing up to 1-µm diamond powder and chemical etching by aqua regia was applied for observing γ/γ′ microstructure. The longitudinal cut specimens were finished either by electrochemical polishing using Struers LectroPol-5 system (electrolyte A3, operated at 45 V for 5 s) or mechanical polishing using colloidal silica solution (particle size 0.04 µm) for the electron backscatter diffraction (EBSD) analysis using a JEOL JSM-6100 scanning electron microscope equipped with EDAX forward scatter detector. Crystallographic orientation in inverse pole figure (IPF) maps refers to the loading direction of the specimen.

3. Results

A) VHCF tests results

VHCF tests were performed on pre-deformed AM1 at 1000 °C with stress ratios of R = − 1 and 0.5 (Figure 4). Under fully reversed condition (R = − 1), both AM1-RTPD-HT1 and AM1-RTPD-Rejuv-HT1 have a similar lifetime compared to the reference "AM1 Bridgman", which was processed with standard heat treatments without pre-deformation [2]. In the tests with a positive ratio of R = 0.5, AM1-RTPD-Rejuv-HT1 performed similarly to the reference AM1-HT1. AM1-RTPD-HT1 failed at a similar life to the reference at R = 0.5 and σ_{max} = 413 MPa and 560 MPa. However, AM1-RTPD-HT1 exhibited a shorter fatigue lifetime of nearly one decade at higher maximum stress condition of σ_{max} = 620 MPa and 551 MPa.

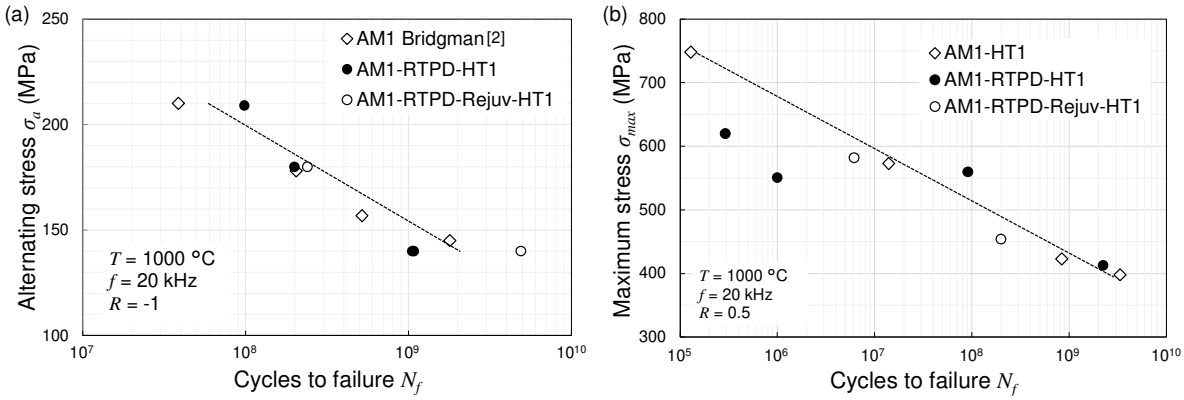

Figure 4. Results of VHCF tests at 1000 °C / f = 20 kHz in the S-N diagram. The alternating stress is plotted as a function of the number of cycles to failure for R = −1 (a). The maximum stress is plotted as a function of the number of cycles to failure for R = 0.5 (b). Data points of AM1 Bridgman in (a) are taken from reference [2].

B) Fractographic observations

Fracture surfaces of specimens after the VHCF test are shown in Figures 5. The fracture plane parallel to the {111} slip system appeared in all specimens. At R = − 1 conditions, the fatal crack started from S-pore close to the cylindrical surface. The rough zone was surrounding S-pores on the fracture surface regardless of applied stress

and lifetime up to ~10^9 cycles (Figure 6(a)). The size of critical S-pore and surrounding rough zone are consistent with previous results from the literature [2]. Also, traces of the microstructure coarsened band were apparent in all AM1-RTPD-HT1 specimens tested at $R = -1$ (see white arrows in Figures 6). In AM1-RTPD-HT1 tested with $R = -1$ and $\sigma_a = 209$ MPa, multiple and isolated S-pores on the fracture surface (Figure 6(b)) presented features similar to the main crack initiating pore (i.e., presence of a rough zone). Multiple S-pores were exposed in the fracture surface of specimens that failed at lower stresses as well.

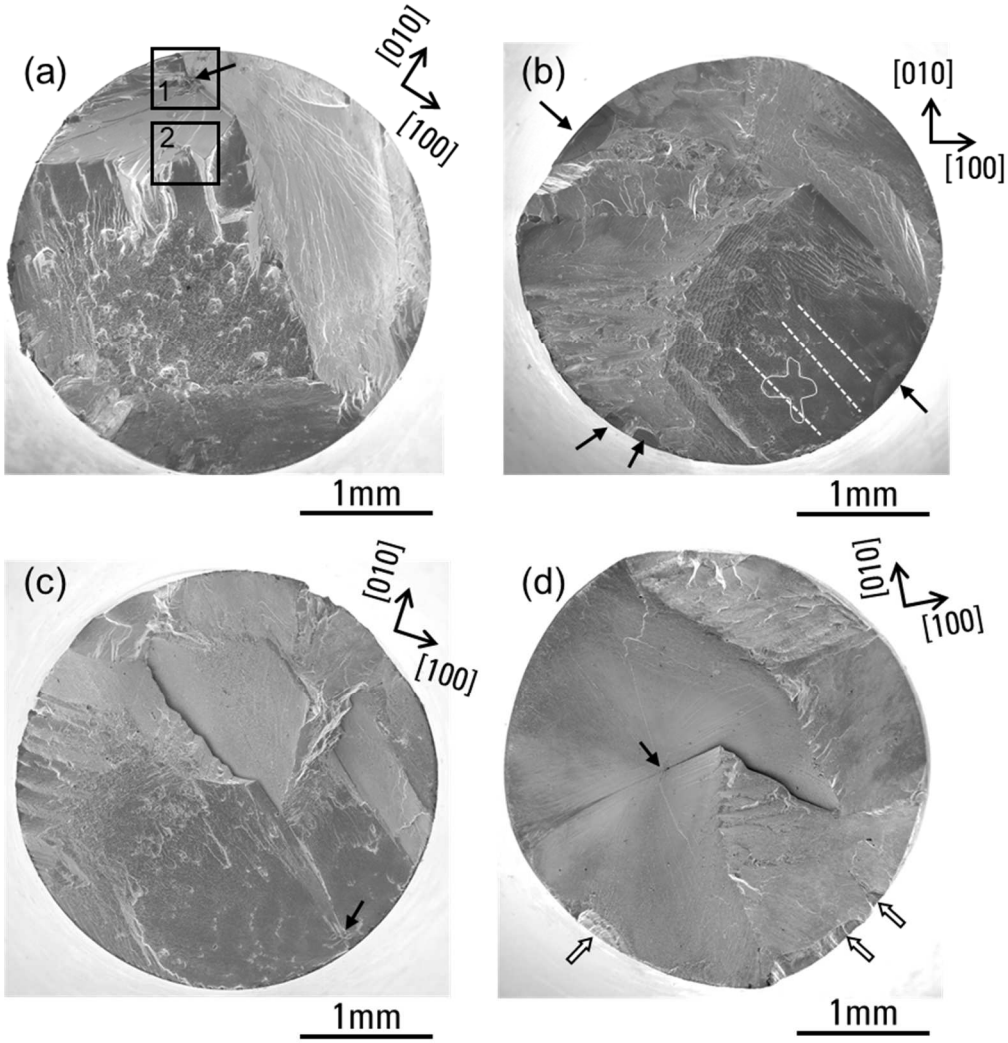

Figure 5. Fractography of AM1-RTPD-HT1 tested at 1000 °C, f = 20 kHz, R = −1, σ_a = 209 MPa (a), AM1-RTPD-HT1 tested at 1000 °C, f = 20 kHz, R = 0.5, σ_{max} = 551 MPa (b), AM1-HT1 tested at 1000 °C, f = 20 kHz, R = 0.5, σ_{max} = 573 MPa (c) and AM1-RTPD-HT1 tested at 1000 °C, f = 20 kHz, R = 0.5, σ_{max} = 560 MPa. Black arrows are pointing at the main crack initiating pore (a, c, d) and surface failure initiating sites (b). White arrows in (d) are pointing at surface cracks. Rectangles 1 and 2 in (a) are shown as magnified images in Figure 6(a) and 6(b), respectively. Dotted lines in (b) are indicating the microstructure coarsened bands. White curve in (b) is showing one of dendrite structures.

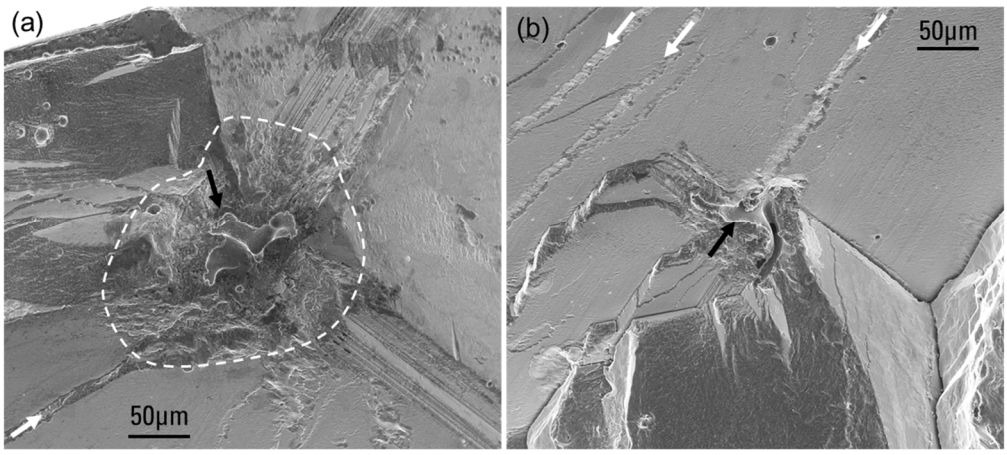

Figure 6. Magnified image of VHCF specimen (AM1-RTPD-HT1) tested at 1000 °C, f = 20 kHz R = −1, σ_a = 209 MPa shown in Figure 5(a). The main crack initiation site is indicated by a black arrow with the rough zone surrounded by the dotted line (a). Another solidification pore on the fracture surface is indicated by a black arrow in (b). White arrows are pointing at microstructure coarsened bands.

AM1-HT1 and AM1-RTPD-Rejuv-HT1 at R = 0.5 and maximum stress lower than 600 MPa also presented an internal crack initiation with the major fracture plane lying on {111} plane, in good agreement with the previous studies [1,2]. Figure 5(c) is an example of an internal crack initiation of AM1-HT1 tested at 1000 °C, f = 20 kHz, R = 0.5, σ_{max} = 573 MPa.

Exception to these trends with a failure starting from the surface was the test performed with the conditions of 1000 °C, f = 20 kHz, R = 0.5, and σ_{max} = 551 MPa (Figure 5(b)). Mode I cracks are initiating from the specimen's surface at locations with an external normal to the specimen's gauge surface of <110> type, as indicated by black arrows in Figures 5(b) and 7(c). At the similar condition of σ_{max} = 560 MPa that showed no effect of pre-deformation on the VHCF life, the specimen had both the internal crack initiation from a pore and surface cracks along ~ <110> type generatrices, as shown in Figure 5(d) by white arrows. The internal crack was directly transferring to crystallographic fracture and no mode I crack propagation stage from this internal pore was observed.

Apart from the cracks of AM1-RTPD-HT1 at R = 0.5, and σ_{max} = 551 MPa, line traces transverse to the specimen's longitudinal direction were also observed (white arrows in Figures 7(c, d)). The same specimen had slip marks parallel to the {111} plane on the surface viewed from a different direction (black arrows in Figure 7(d)). Such {111} slip traces are similar to those previously observed at the specimen's surface just after pre-deformation or after creep tests at temperatures above 950 °C [8,15]. AM1-RTPD-HT1 at R = 0.5 and σ_{max} = 620 MPa had crack initiation from the surface as well. This specimen showed a very high density of {111} slip traces near fracture surface (Figure 8(a)) compared to specimen tested at σ_{max} = 551 MPa.

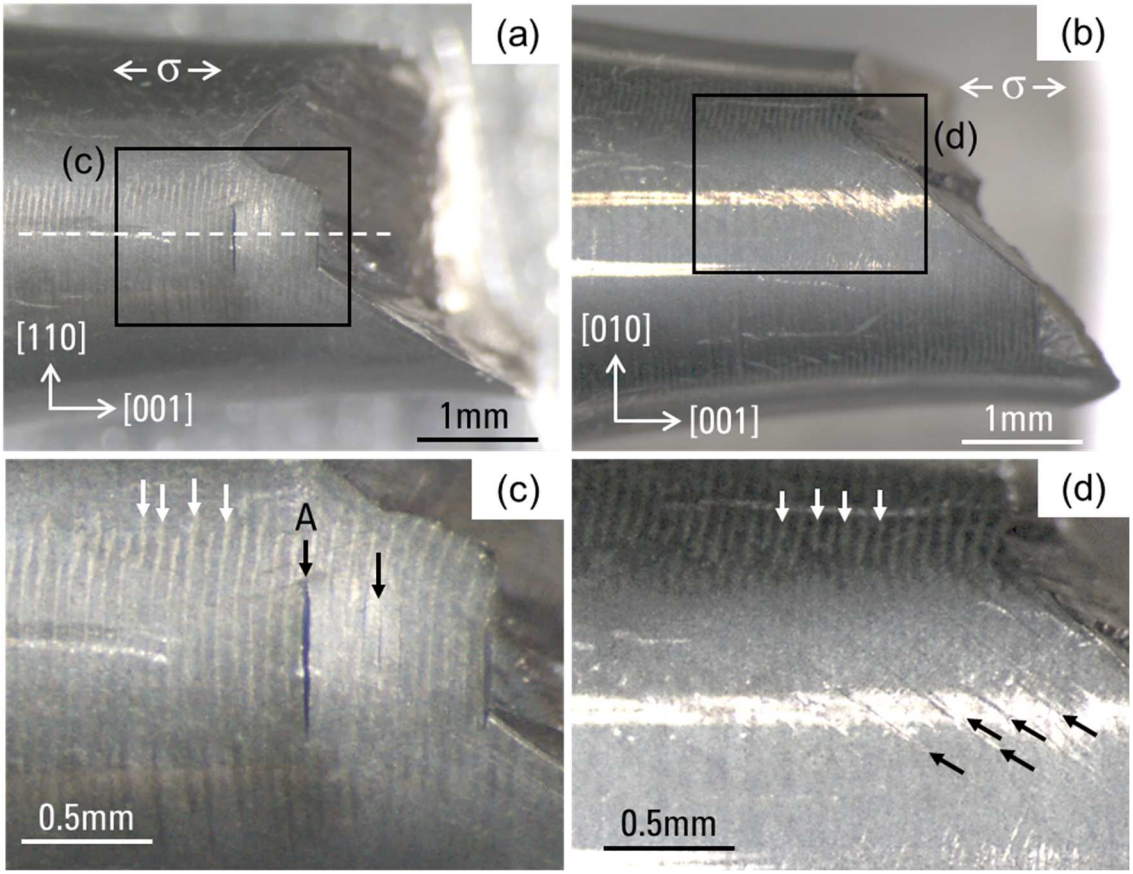

Figure 7. Appearances of the VHCF specimen (AM1-RTPD-HT1) tested at 1000 °C, f = 20 kHz, R = 0.5, σ_{max} = 551 MPa from two different directions (a, b). Rectangles in (a) and (b) are shown in (c) and (d), respectively. Black arrows in (c) are pointing at surface cracks. The microstructure of crack A is presented in Figures 11 and 12. Black arrows in (d) are showing {111} slip traces appearing on the cylindrical surface. White arrows in (c) and (d) are line traces transverse to the loading direction. Dotted line in (a) is the cutting plane for microstructure observation (see Figure 11).

The transverse line traces and {111} slip bands also appeared on the surface of AM1-HT1 (R = 0.5 / σ_{max} = 582 MPa), AM1-RTPD-HT1 at lower applied stress (R = 0.5 / σ_{max} = 413 MPa in Figure 8(b)), and AM1-RTPD-Rejuv-HT1 (R = 0.5 / σ_{max} = 573 MPa in Figure 8(c) and R = 0.5 / σ_{max} = 454 MPa in Figure 8(d)). AM1-HT1 and AM1-RTPD-Rejuv-HT1 had by far a lower number of {111} slip bands compared to AM1-RTPD-HT1. Surface micro-cracks were also observed in some of those specimens at the intersection of two slip bands; however, the failure came from an internal crack initiation site (i.e., an S-pore). Non-fatal surface cracks that do not lead to the failure have been reported in the thesis by Cervellon [19].

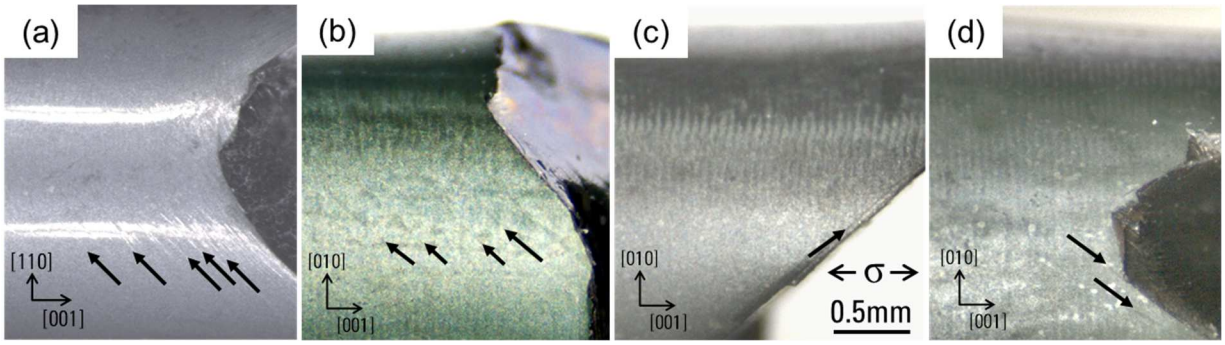

Figure 8. Appearances of the VHCF specimens tested at 1000 °C, f = 20 kHz, R = 0.5. AM1-RTPD-HT1 at σ_{max} = 620 MPa (a), AM1-RTPD-HT1 at σ_{max} = 413 MPa (b), AM1-RTPD-Rejuv-HT1 at σ_{max} = 582 MPa (c), and AM1-RTPD-Rejuv-HT1 at σ_{max} = 454 MPa (d). Black arrows are pointing at {111} slip traces.

C) Microstructure characterization of the specimen's longitudinal sections

Precipitate scale observations of the microstructure coarsened bands are shown in Figure 9. Figures 9(a, b, d) were obtained by observing a primary dendrite core inside of the specimen. γ′ precipitates in the specimen tested at R = −1 / σ_a = 209 MPa (Figure 9(a)) had coarsened more than the ones in the specimen tested in R = 0.5 (Figure 9(b)), which is simply because the overall duration of this test was longer. Although microstructure evolution had not proceeded much, dislocation traces were observed in the microstructure coarsened band of the specimen tested with R = 0.5 / σ_{max} = 551 MPa (magnified image in Figure 9(d)), whereas they were not observed in R = −1 / σ_a = 209 MPa (Figure 9(a)). A notable difference between dendritic cores/interdendritic areas at the bulk has not been investigated.

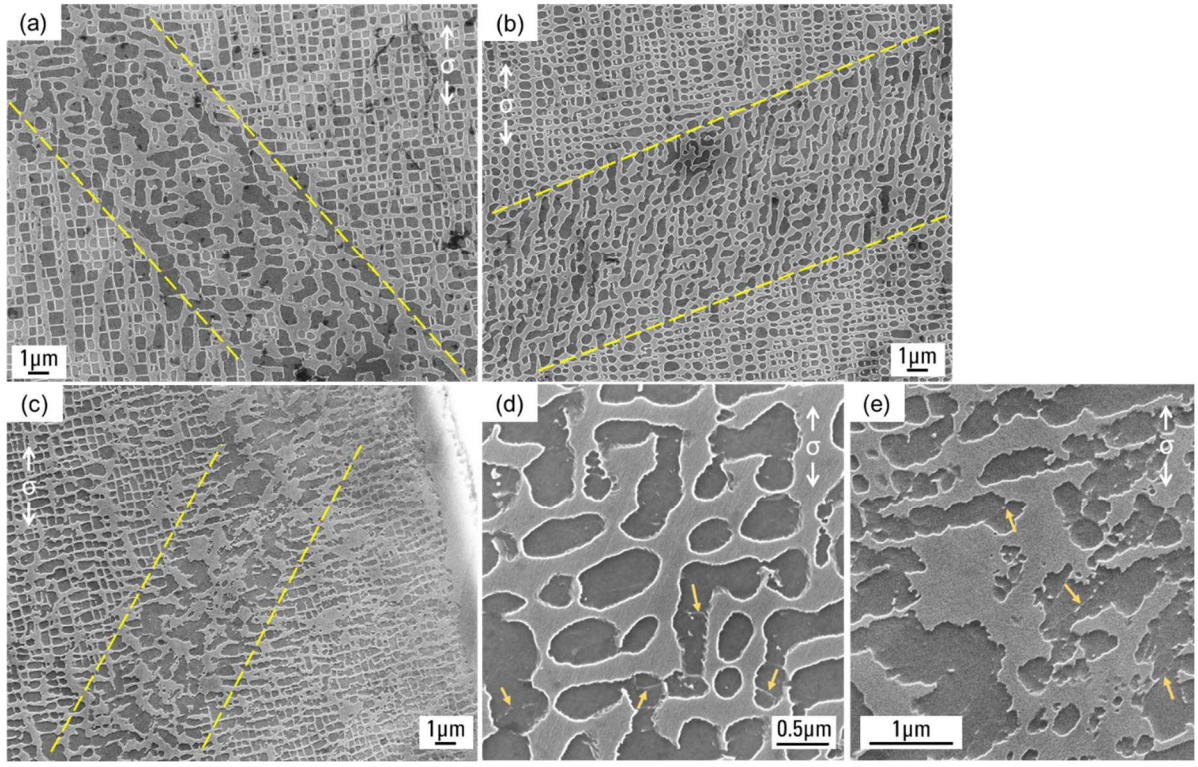

Figure 9. Precipitate scale microstructure observed in longitudinal cross section of AM1-RTPD-HT1 specimens after tests at 1000 °C, f = 20 kHz. (a) R = −1, σ_a = 209 MPa, failed at 9.8 × 10^7 cycles, (b-e) R = 0.5, σ_{max} = 551 MPa, N_f = 1.0 × 10^6 cycles. Microstructure inside the specimen and that close to the

specimen's surface are shown in (b) and (c), respectively. (d) and (e) are magnified images inside the microstructure coarsened band of (b) and (c), respectively. Arrows are pointing at dislocation traces in the γ′ phase. Dotted lines are indicating the microstructure coarsened bands.

Close to the specimen's surface, microstructure coarsening proceeded much faster inside the band (Figure 9(c)) with a very high density of dislocation traces (Figure 9(e)). Because of heavy deformation close to the surface, the dendritic structure could not be identified. These specimens did not have intermetallic phases other than γ matrix and γ′ precipitates (i.e., TCP phases). AM1 is indeed known to be an alloy with a very stable microstructure without TCP precipitation after over 400 h of creep test at 1050 °C [15].

Figures 10(a, b) are showing γ/γ′ microstructure around an S-pore on the fracture surface associated with a rough zone. Like in previous studies [1,4], a high density of shear traces and disturbed γ/γ′ microstructure were observed below the rough zone (Figure 10(b)). Figure 10(c) is an example of an S-pore where cracks are propagating along recrystallized grains (see Figure 10(d)), which will become the rough zone and can be considered as an intermediate stage before failure [4].

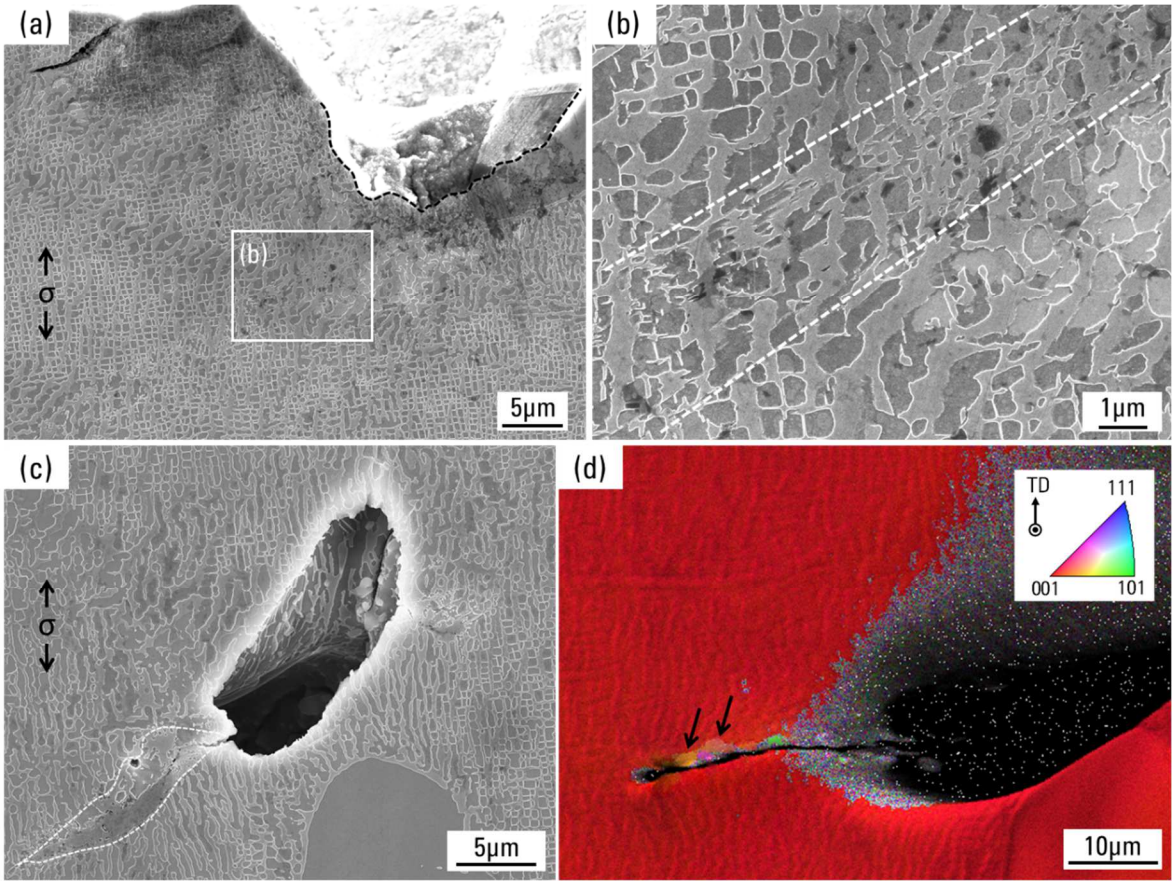

Figure 10. Microstructure observed along longitudinal cut of AM1-RTPD-HT1 specimen tested at 1000 °C, f = 20 kHz, R = −1, σ_a = 209 MPa. (a) The area near the fracture surface with S-pore exhibiting the rough zone indicated by the dotted curve. (b) Magnification of the rectangle in (a) showing microstructure shearing in between dotted lines. (c) S-pore inside the specimen. The dotted curve is showing the evolved microstructure with crack propagation. (d) IPF map of the area around the crack in (c) superimposed on forward scatter detector signal. Arrows are showing recrystallized grains along the crack path.

Figures 11(a) is showing the low magnification microstructure at the surface of AM1-RTPD-HT1 specimen tested at 1000 °C, f = 20 kHz, R = 0.5, σ_{max} = 551 MPa (cutting plane before polishing is shown in Figure 7(a)). Despite a very short test duration (~ 50 s), multiple surface cracks were observed, as well as the microstructure coarsened bands indicated by dotted lines in the same figure to help the reader. Figure 11(b) is a crystallographic orientation map superimposed to an image quality (IQ) map obtained by EBSD analyses. Three surface recrystallization areas are in this IPF + IQ map. A darker area in an IQ map corresponds to an area with a higher dislocation density that decreases diffraction quality. Two areas on the right and left are associated with initiated cracks. The recrystallized area located in the middle is a potential third crack initiation site (see arrow in Figure 11(b)). The specimen's surface layer of ~30 µm in thickness has dark areas and lines, as observed in Figure 11(b). The bands with disturbed microstructure, like the one shown in Figure 9(c), are observed in this layer. Figure 11(c) shows the crack filled with oxide and surrounded by the γ′-depleted zone all along the crack path up to the tip.

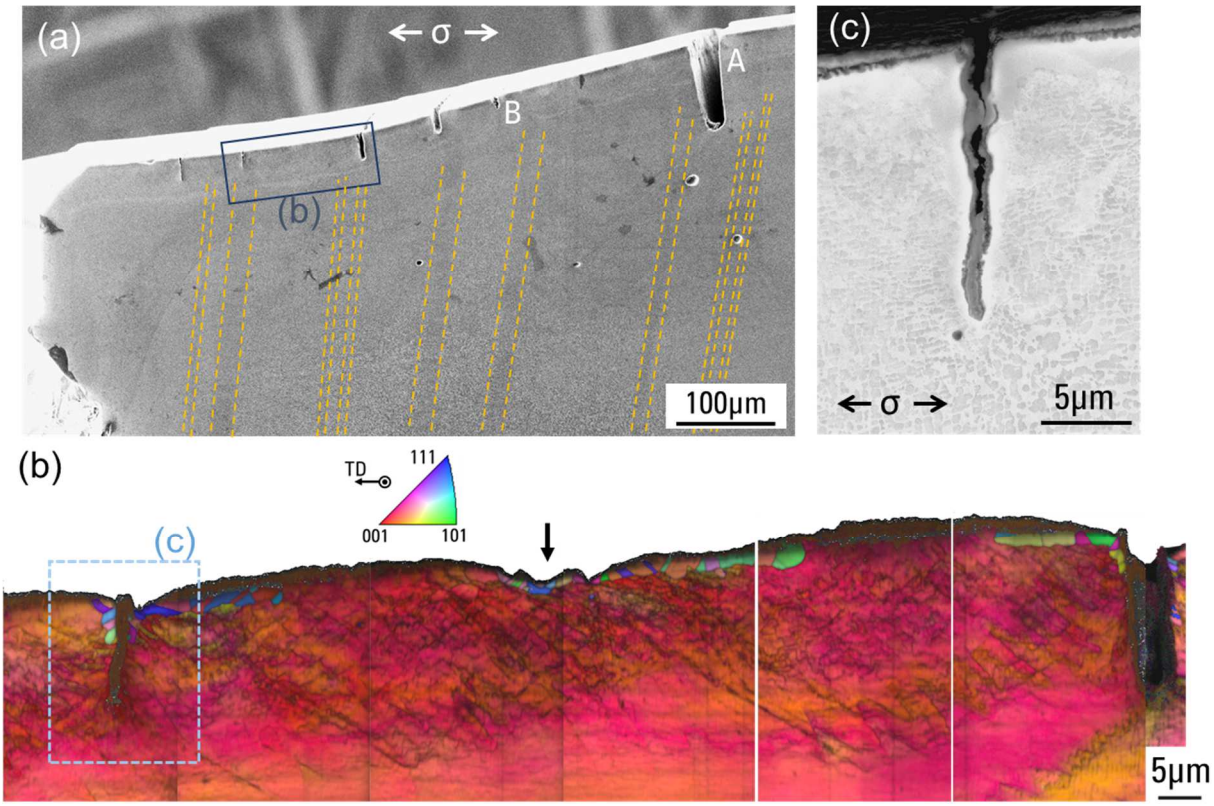

Figure 11. Microstructure observed along longitudinal cross section (~ (110) plane) of AM1-RTPD-HT1 specimen tested at 1000 °C, f = 20 kHz, R = 0.5, σ_{max} = 551 MPa. (a) Low magnification image taken from the area with surface cracks. Dotted lines are indicating the microstructure coarsened bands. (b) Merged IPF + IQ maps at the surface layer indicated by the rectangle in (a). Arrow is pointing at the recrystallized area without crack. (c) Backscatter electron image of the area indicated by the rectangle in (b).

Other cracks marked as A and B in Figure 11(a) are presented in Figure 12 with higher magnification and IPF maps. These cracks have a larger opening (> 3µm) with crack tips not filled with oxides, whereas the oxides are filling the crack with a smaller opening (Figure 11(c), ~1 µm). The crack on the right in Figure 11(b) has the same

features as cracks A and B (i.e., large opening and no oxide filling). Recrystallized grain was not observed around crack A with the largest opening (Figure 12(c)). Lattice rotation at the tip of this crack A indicates the existence of extreme stress concentration. The IPF map in Figure 12(d) shows recrystallized grains surrounding crack B. At the tips of both cracks A and B, slip bands can be observed in secondary electron images and IPF maps. When these IPF maps are superimposed to an IQ map, slip bands appear as dark lines due to a high dislocation density. It should be noted that slip bands in the sub-surface layer and at the crack tips are different from the slip bands introduced during pre-deformation. All of these slip bands are different from the microstructure coarsened bands that formed during aging treatments.

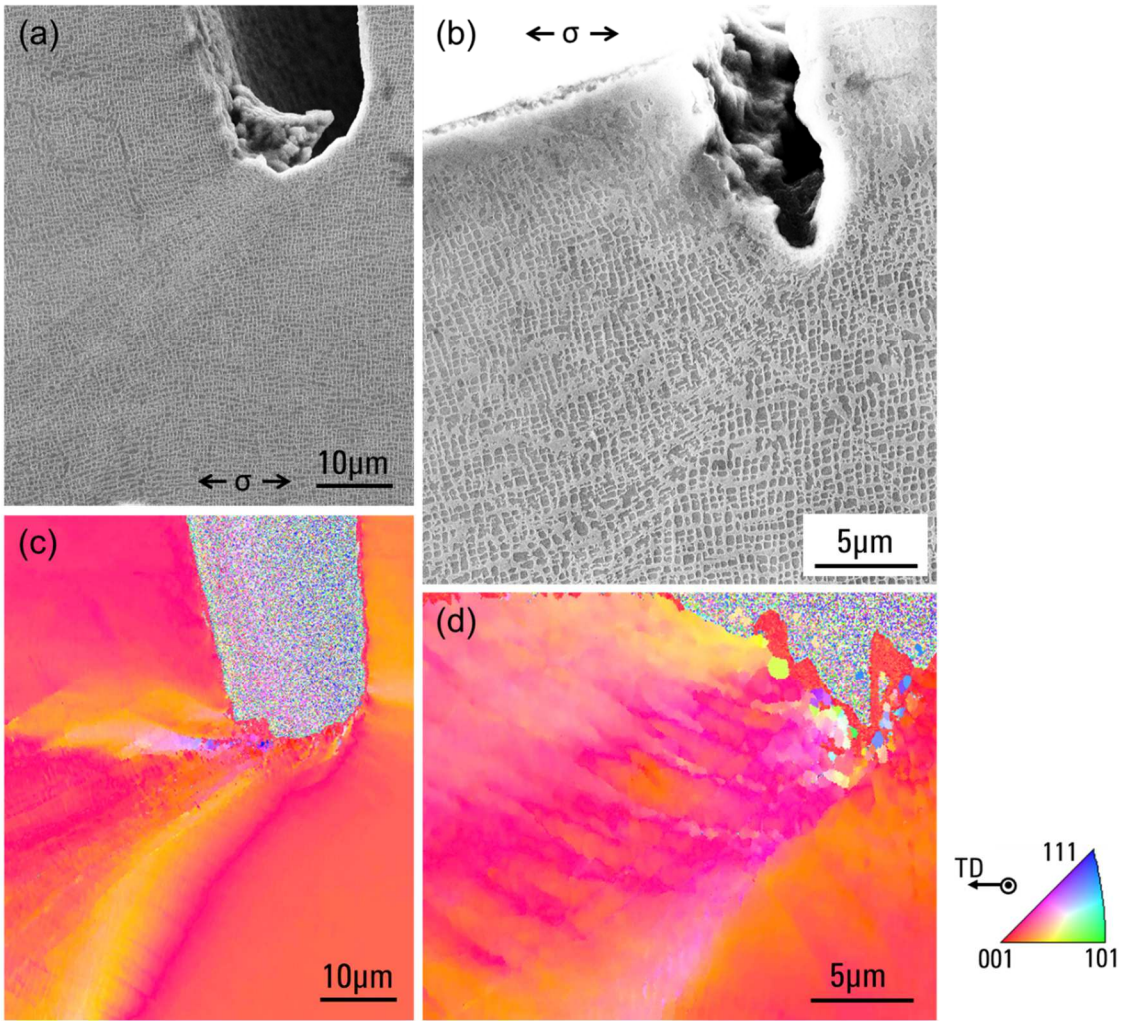

Figure 12. Microstructure observed along longitudinal cross section (~ (110) plane) of AM1-RTPD-HT1 specimen tested at 1000 °C, f = 20 kHz, R = 0.5, σ_{max} = 551 MPa, failed at 1.0 × 10^6 cycles. (a, b) Secondary electron images showing γ/γ′ microstructure. (c, d) IPF maps in the same area as (a, b). (a, c) and (b, d) are corresponding to the cracks indicated as A and B in Figure 11(a), respectively.

4. Discussion

A) Effect of pre-deformation in fully reversed condition $R = -1$

In the previous study, stereological analyses were performed on void/pore size and counts in AM1-RTPD-HT1

[15]. Increase in void size and density induced by pre-deformation before aging treatments has been evidenced [15]. Since void/pore size is the critical factor controlling the VHCF durability in the Ni-based SX superalloys under fully reversed condition [2,5], the pre-deformed material having a lifetime similar to non-pre-deformed material seems contradictory.

Recalling that both reference and AM1-RTPD-HT1 are produced by the Bridgman SX casting method with similar casting parameters, primary dendrite arm spacings, S-pores, and eutectics are assumed to be comparable in these materials in the as-solutioned state. Thus, the probability of having a critical S-pore within the gauge center section of the VHCF specimens are equivalent. In the previous study, larger voids' counts and size distribution are not significantly different among the two materials, AM1-HT1 and AM1-RTPD-HT1 [15]. Diameter of S-pores in AM1-RTPD-HT1 was within the range of reference data taken from the previous study [2], as described in the experimental procedures. Moreover, it has already been shown that increased void size by over-aging did not affect the VHCF life of CMSX-4 tested under similar testing conditions [1]. An increased number of smaller H/D-pores by pre-deformation (compare Figures 3(a, b)) is not an essential factor controlling the VHCF life of Ni-based SX superalloys under fully reversed conditions, in good agreement with a previous analysis by Cervellon et al. [1].

The fracture surface of all AM1-RTPD-HT1 specimens after VHCF tests exhibited either a {111} plane or pattern of the microstructure coarsened band. Moreover, in the fully reversed VHCF conditions, multiple S-pores were exposed on the fracture surface with the surrounding rough zone (Figure 6) and were connected to microstructure coarsened bands. These imply that, although pre-deformation may not affect the initiation of the fatal crack and overall durability in these conditions, the microstructure coarsened bands and pores lying on the bands remained as preferable damaging sites that assist crack propagation up to the final fracture. By increasing the duration of VHCF tests at $R = -1$ (tests in excess of 10^{10} cycles), an effect of pre-deformation on VHCF life might be observed, resulting from a prolonged time to allow sufficient microstructure evolution within the coarsened bands.

In the previous studies performed at Institut Pprime, it was almost impossible to identify secondary cracks outside of the main crack initiation site of specimen tested at $R = -1$ [1–5,11]. Once again, slip bands intersecting with S-pores can help pore growth during subsequent aging treatment, but it did not change pore size drastically. Slight difference in S-pore size was confirmed to be negligible because AM1-RTPD-HT1 showed similar VHCF performance to the non-pre-deformed AM1. Contrarily to the previous studies, several pores were triggering recrystallization in AM1-RTPD-HT1 at σ_a = 209 MPa, like in Figure 10(c). Those pores were mostly connected to the microstructure coarsened band. The γ/γ′ microstructure around this pore and the recrystallized area is coarser compared to the other areas. The micro shearing had probably started from the pore, and it created a local intense strain field. Once the local plastic deformation reaches a certain amount, it accelerates the microstructure evolution and activates the recrystallization. Cervellon et al. have already presented this mechanism in the same VHCF conditions [4]. In the non-pre-deformed specimens, S-pore with surrounding recrystallized area was only present at the fracture surface [2].

From the present study, it is suggested that coarsened and degraded γ/γ′ microstructure surrounding S-pore favors the primary process (microstructure shearing) of a crack initiation. Some S-pores in the non-pre-deformed material have coarse microstructure nearby due to sub-grain boundaries and eutectics. Indeed, S-pore connected to the microstructure coarsened band is a favorable site for this crack initiation process in the pre-deformed material. These degraded γ/γ′ microstructures may have locally higher dislocation density before applying load that assisted the shearing process [8], which is different from pre-rafted microstructure that does not affect VHCF life at the same conditions [1]. Therefore, the number of cycles required to initiate a fatal crack is the same regardless of pre-deformation; however, the number of potential primary crack initiating pore is increased by the pre-deformation.

B) Enhanced shearing and recrystallization at positive stress ratio condition, $R = 0.5$

In previous studies, Cervellon et al. have shown that the γ/γ′ microstructure (morphology and size) controls the VHCF life at 1000 °C of Ni-based SX superalloys when a high mean stress is superimposed to the alternating stress [1,11]. VHCF damages include a creep contribution when the material is exposed to high-temperature and a tensile stress for all testing periods [11,20]. At a very high strain rate in the tensile deformation, a degraded γ/γ′ microstructure presents lower yield stress than the optimal cuboidal microstructure [1,21–24]. In the present study, the microstructure coarsened bands have a higher dislocation density both in bulk (Figure 9(d)) and especially at the surface layer (Figure 9(e)). In addition, during creep at 850 °C / 500 MPa or 1050 °C / 200 MPa, microstructure shearing occurred much more frequently inside the microstructure coarsened bands [14]. Therefore, fatigue damage mechanisms can proceed faster inside the microstructure coarsened bands when the creep damage is active, and the VHCF life of pre-deformed AM1 may decrease at high mean stress conditions. Furthermore, initial dislocations introduced by a combination of pre-deformation and subsequent aging treatments can enhance dislocation penetration from the matrix into the precipitates that accelerate the damaging process.

The shorter VHCF lifetime of AM1-RTPD-HT1 compared to AM1-HT1 at the conditions $R = 0.5$ / σ_{max} = 551 MPa and σ_{max} = 620 MPa is clearly the consequence of pre-deformation. However, unlike other specimens that exhibited internal crack initiation, AM1-RTPD-HT1 presented multiple cracks from the surface and did not have an internal crack from the creep void. The reason for the absence of creep damage is because fatigue loading time was so short (less than 1 min) that the γ′-rafting and creep void growth did not have sufficient time to occur (Figure 9(b)). A unique feature of AM1-RTPD-HT1 is a greater number of the {111} slip band traces shown in Figures 7(d) and 8 compared to that in either AM1-HT1 or AM1-RTPD-Rejuv-HT1, although the test duration of AM1-RTPD-HT1 was by far shorter at high mean stress condition. With a very high density of dislocations at the surface layer shown in Figure 11(b) and a high density of the slip band traces on the surface, the sub-surface microstructure can be considered as the key in this specimen's fatigue failure.

The average spacing between transverse traces in Figure 7(a) is 66 μm, and that of cracks observed in Figure 11(a) is 71 μm (recrystallized area pointed by the arrow in Figure 11(b) is counted as a “close-to-initiated-crack”). Recrystallized layers in Figure 11(b) are observed as the transverse traces at lower magnification. These facts

confirm that the surface recrystallizations in the pre-deformed specimen are linked to the transverse traces. The transverse band traces along ~ <110> type generatrices formed in all specimens tested at R = 0.5 as a result of preferential slip accumulation and stress concentration created by the alternating stress, and possibly because of elastic anisotropy of SX specimen [25,26]. Strongly marked {111} slip traces and their intersection with the transverse traces increase the specimen's surface roughness. Hence, intersection of two slip traces on the surface of the pre-deformed material suffers intense stress concentration and triggering surface recrystallization that leads to very rapid failure.

The recrystallized layer in Figure 11(b) is limited to only one-grain thickness. Two deeper cracks in Figure 11(b) and the largest one in Figure 12(c) do not have recrystallized grains up to their crack tips. In the same two cracks observed in Figure 11(b), the recrystallized layer below the surface along the crack path has a depth of ~10 μm. This recrystallization depth is the same as the crack depth shown in Figure 12(d), which has recrystallized grains at its tip. This recrystallized depth suggests that recrystallization causes crack initiation and mode I crack opening at the surface, but it is not necessary for cracks to propagate further. Crack tip plasticity shown as slip bands in Figure 12(a, c) is a typical one observed in mode I crack transitioning into mode II crack [27,28] and is enough to ensure further crack propagation. Once the crack penetrates the deformed layer, crystallographic cracking take place until failure. Fracture surface in Figures 5(b) and 7(a, b) is showing fracture planes similar to what has been shown in the literature [29–32].

Figure 13 schematically represents the crack initiation mechanism that occurred in AM1-RTPD-HT1 at 1000 °C, f = 20 kHz, R = 0.5, σ_{max} = 551 MPa and σ_{max} = 620 MPa. The microstructure coarsened bands lying on {111} plane facilitates shearing (see microstructure in Figure 9(c-e) and schematic illustration in Figure 13(b)). This leads to {111} slip traces at the specimens' surface, as observed in Figure 7(d). Slip trace intersection with the specimen's <110> generatrix leads to a greater stress concentration due to the slip accumulation and the creation of a locally greater roughness (Figures 13(b, c)). The deformed layer is created underneath the stress concentration area, and a high density of dislocations is accumulated at the transverse trace (Figure 13(d)). Recrystallization is subsequently triggered at the surface layer (Figure 13(e)), which can be assisted by oxidation (there is also 45 min of soak at 1000 °C before the application of the alternating/mean stress used for specimens' emissivity stabilization, ensuring a reliable temperature control during the tests) that leads to an Al depletion and very local γ′ dissolution [33,34]. Finally, mode I crack opening starts at the recrystallized area and propagates like other typical fatigue mode I cracks (Figure 13(f)) [27,28]. Once these mode I micro-cracks become long enough, they bifurcate into a mode II crack, and specimen ultimately fails with crystallographic cracking (see fracture surface in Figure 5(b)) [29–32].

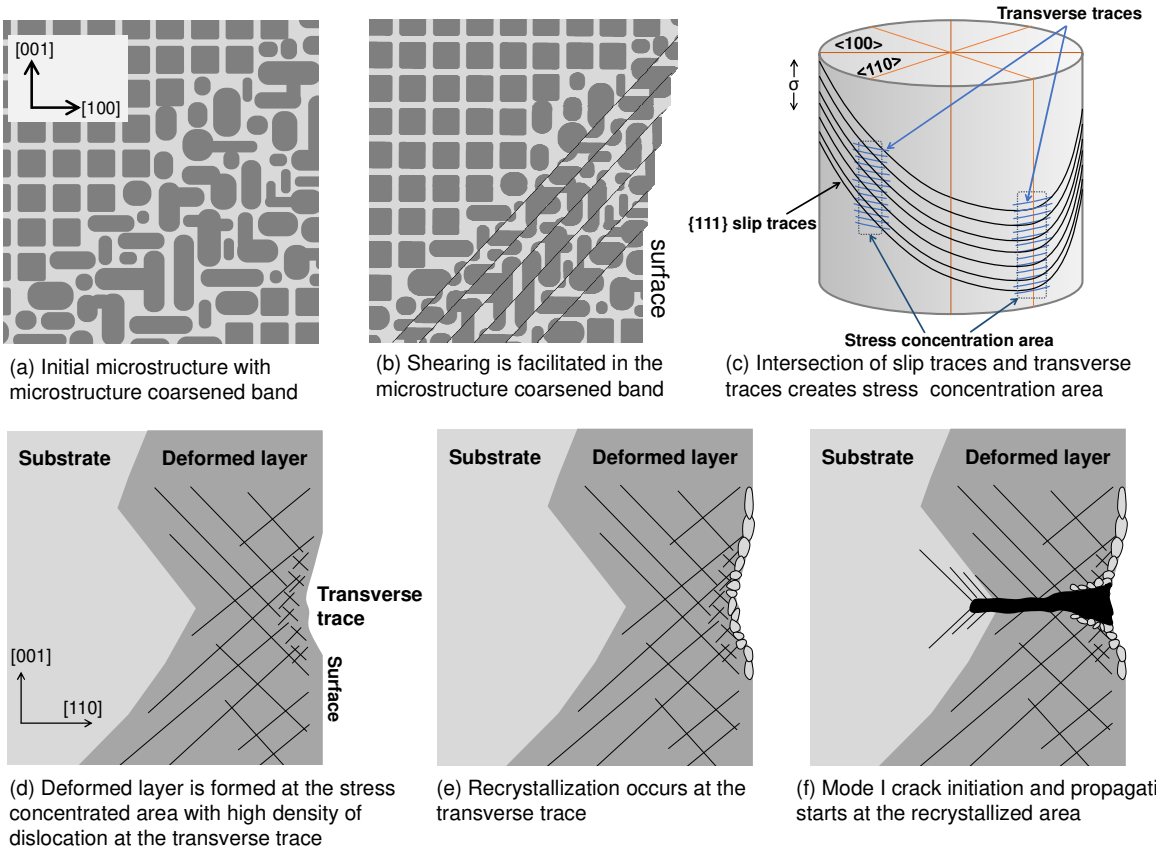

(a) Initial microstructure with microstructure coarsened band

(b) Shearing is facilitated in the microstructure coarsened band

(c) Intersection of slip traces and transverse traces creates stress concentration area

(d) Deformed layer is formed at the stress concentrated area with high density of dislocation at the transverse trace

(e) Recrystallization occurs at the transverse trace

(f) Mode I crack initiation and propagation starts at the recrystallized area

Figure 13. Schematic illustration of the crack initiation mechanisms in pre-deformed Ni-based SX superalloys at high temperature and high applied mean stress VHCF test.

During isothermal creep tests, local microstructure shearing in the band was more apparent in the creep conditions with higher stress [14]. This is consistent with the fact that shearing inside the band was facilitated in the pre-deformed material during the VHCF test at a positive ratio condition with high maximum stress. According to a previous study from the authors, time dependent creep damage should be accumulated faster inside the microstructure coarsened band and causes earlier failure [15]. However, at the lower maximum stress condition (~400 MPa), the VHCF lifetime was not affected by the pre-deformation in the S-N diagram (Figure 2(b)). Fatigue tests with a lower applied mean stress can be an option to clarify the possibility of localized creep damage accumulation within the band. Decreasing the testing frequency can be another option to check this possibility; however, a lower strain rate may change the active deformation and damage mechanisms [11]. Overall, the difference in VHCF life between pre-deformed and non-pre-deformed specimens at this condition (σ_{max} ~400 MPa) remains within the standard variability observed among all the data generated at Institut Pprime using different Ni-based SX superalloys and this machine (over 300 VHCF test results at 1000 °C, including different R ratios).

Another remaining question is whether the pre-deformation effect on the VHCF life gradually increases with an increase of σ_{max} from ~400 MPa to ~550 MPa or if there is a critical mean stress that activates a transition in failure mechanism from an internal to a surface site according to the mechanism shown in Figure 13. Earlier in this section, we explained that facilitated shearing in the microstructure coarsened band is an important factor of

decreased VHCF life. Several studies on Ni-based SX superalloys have shown that the yield strength becomes more sensitive to the alloy's precipitate size as the strain rate increases [1,21–24]. Because coarsened microstructure locally has lower shear resistance, pre-deformed material should undergo higher plastic strain magnitude within the microstructure coarsened bands, creating rough surface that critically affects fatigue life. This is also a reason why only few slip traces were observed very close to the fracture surface of AM1-HT1 and AM1-RTPD-Rejuv-HT1 (see Figure 8). Meanwhile, AM1-RTPD-HT1 at lower mean stress presented more {111} slip traces (Figure 8(b)), which means slip activation is still favorable but without any impact on the fatigue life. Surprisingly, AM1-RTPD-HT1 at σ_{max} = 560 MPa performed better that at σ_{max} = 551 MPa. The specimen tested at σ_{max} = 560 MPa presented both internal and surface cracks (Figure 5(d)). This means that the two failure modes (internal and surface) are competing, but the surface crack did not grow enough to further control the ultimate failure. It is therefore suggested that σ_{max} ~550 MPa could be border condition above which the failure mechanism explained in Figure 13 become active. AM1-RTPD-HT1 at σ_{max} = 620 MPa had high density of slip traces near the fracture surface (Figure 8(a)), meaning that γ/γ′ microstructure shearing is strongly favorable at a higher maximum stress condition.

The border condition for drastic fatigue life reduction is possibly determined by the sensitivity to the microstructure shearing and resulting surface roughness that activates surface recrystallization. In another words, at a higher maximum stress condition, microstructure shearing becomes locally more important in coarsened microstructure bands and the local level of microstructure degradation within a coarsened band can be a determining factor of the overall VHCF lifetime at R = 0.5, and more generally, at high R ratios at this temperature. A reliable quantification would require a larger number of VHCF tests at around suspected border conditions and it remains a field for further investigation.

C) VHCF life restoration by rejuvenation heat treatment

Like creep properties presented in one of our previous studies [14], rejuvenation treatment after pre-deformation successfully restored VHCF properties in all conditions tested in this study. It was especially effective in the positive stress ratio condition where pre-deformation leads to a debit in VHCF lifetime at high maximum stresses (σ_{max} > 550 MPa). This result supports the fact that a coarsened microstructure affects fatigue life when a high mean stress is applied at high temperatures [1]. On the other hand, further S-pore growth by additional high-temperature re-solution treatment and stress relaxation, which is one of the risks using a rejuvenation treatment, had not occurred and rejuvenation showed no effect on the VHCF life of the material. The effectiveness of rejuvenation treatment is demonstrated in VHCF behavior in addition to the creep properties [14].

5. Conclusions

Fatigue properties of AM1 Ni-based single crystal superalloy with prior plastic deformation applied between solution and aging treatment has been tested in the very high cycle domain at 1000 °C using an ultrasonic fatigue machine (f = 20 kHz). The main conclusions established in this study are:

- VHCF lifetime and main crack initiation mechanisms in fully reversed (R = −1) conditions were not affected

by either the microstructure coarsened band or the increased density of smaller pores in pre-deformed material. Fractographic and microstructural observations on pre-deformed material showed multiple pores presenting the primary process of crack initiation associated with local recrystallization around them.

- Pre-deformation decreased the VHCF lifetime by more than a decade at a positive stress ratio (R = 0.5) and high mean stress condition. The microstructure coarsened band in the pre-deformed material facilitated γ/γ′ microstructure shearing at a very high strain rate in the ultrasonic fatigue test, resulting in {111} slip traces appearing on the specimens' surface. The accumulated slip along <110>-type generatrices of the specimens led to a locally higher density of dislocations and stress concentration, hence triggering surface recrystallization. Mode I surface cracks were initiated from the recrystallized area and then transitioned to crystallographic cracking, leading to the earlier failure by nearly one decade compared to the specimen without pre-deformation.
- Rejuvenation treatment can restore VHCF lifetime at a positive stress ratio condition and does not affect fatigue life in all the other conditions tested in this study.

Acknowledgments

Safran Aircraft Engines is acknowledged for its financial support, providing material, and continuous interest in the subject. Mr. Florent Mauget (Institut Pprime, France) and Dr. Alice Cervellon (University of California, Santa Barbara, CA, USA) are acknowledged for their technical support and suggestions. Dr. Samuel Hémery (Institut Pprime) is acknowledged for his technical support. Mr. Jacques Lefort (Institut Pprime) is gratefully acknowledged for designing the specimen geometry specifically for pre-deformation and operating complex specimen preparations. Institut Pprime gratefully acknowledges "Contrat de Plan Etat - Région Nouvelle-Aquitaine (CPER)" as well as the "Fonds Européen de Développement Régional (FEDER)" for their financial support to the reported work. Part of this study was supported by the Nouvelle-Aquitaine French region through the ECOREVE project (project number 2018-1R10122). This study is also part of the "Self-Heating" ANR-Safran-Naval group research chair (Grant # ANR-20-CHIN-0002) involving the Safran Companies, Naval group, ENSTA Bretagne (IRDL) and Institut Pprime.

References

[1] Cervellon A, Cormier J, Mauget F, Hervier Z. VHCF life evolution after microstructure degradation of a Ni-based single crystal superalloy. Int J Fatigue 2017;104:251–62. https://doi.org/10.1016/j.ijfatigue.2017.07.021.

[2] Cervellon A, Cormier J, Mauget F, Hervier Z, Nadot Y. Very High Cycle Fatigue of Ni-Based Single-Crystal Superalloys at High Temperature. Metall Mater Trans A 2018;49:3938–50. https://doi.org/10.1007/s11661-018-4672-6.

[3] Bortoluci Ormastroni LM, Mataveli Suave L, Cervellon A, Villechaise P, Cormier J. LCF, HCF and VHCF life sensitivity to solution heat treatment of a third-generation Ni-based single crystal superalloy. Int J Fatigue 2020;130:105247. https://doi.org/10.1016/j.ijfatigue.2019.105247.

[4] Cervellon A, Hémery S, Kürnsteiner P, Gault B, Kontis P, Cormier J. Crack initiation mechanisms during

very high cycle fatigue of Ni-based single crystal superalloys at high temperature. Acta Mater 2020;188:131–44. https://doi.org/10.1016/j.actamat.2020.02.012.

[5] Bortoluci Ormastroni LM, Utada S, Rame J, Mataveli Suave L, Kawagishi K, Harada H, et al. Tensile, low cycle fatigue and very high cycle fatigue characterizations of advanced single crystal nickel-based superalloys. In: Tin S, Hardy M, Clews J, Cormier J, Feng Q, Marcin J, et al., editors. Superalloys 2020, Springer International Publishing; 2020, p. 341–51. https://doi.org/10.1007/978-3-030-51834-9_33.

[6] Anton DL, Giamei AF. Porosity distribution and growth during homogenization in single crystals of a nickel-base superalloy. Mater Sci Eng 1985;76:173–80. https://doi.org/10.1016/0025-5416(85)90091-6.

[7] Link T, Zabler S, Epishin A, Haibel A, Bansal M, Thibault X. Synchrotron tomography of porosity in single-crystal nickel-base superalloys. Mater Sci Eng A 2006;425:47–54. https://doi.org/10.1016/j.msea.2006.03.005.

[8] Hamadi S, Hamon F, Delautre J, Cormier J, Villechaise P, Utada S, et al. Consequences of a Room-Temperature Plastic Deformation During Processing on Creep Durability of a Ni-Based SX Superalloy. Metall Mater Trans A 2018;49:4246–61. https://doi.org/10.1007/s11661-018-4748-3.

[9] Kontis P, Li Z, Collins DM, Cormier J, Raabe D, Gault B. The effect of chromium and cobalt segregation at dislocations on nickel-based superalloys. Scr Mater 2018;145:76–80. https://doi.org/10.1016/j.scriptamat.2017.10.005.

[10] Kontis P, Li Z, Segersäll M, Moverare JJ, Reed RC, Raabe D, et al. The Role of Oxidized Carbides on Thermal-Mechanical Performance of Polycrystalline Superalloys. Metall Mater Trans A 2018;49:4236–45. https://doi.org/10.1007/s11661-018-4709-x.

[11] Cervellon A, Yi JZ, Corpace F, Hervier Z, Rigney J, Wright PK, et al. Creep, Fatigue, and Oxidation Interactions During High and Very High Cycle Fatigue at Elevated Temperature of Nickel-Based Single Crystal Superalloys. In: Tin S, Hardy M, Clews J, Cormier J, Feng Q, Marcin J, et al., editors. Superalloys 2020, Springer International Publishing; 2020, p. 185–95. https://doi.org/10.1007/978-3-030-51834-9_18.

[12] Steuer S, Hervier Z, Thabart S, Castaing C, Pollock TM, Cormier J. Creep behavior under isothermal and non-isothermal conditions of AM3 single crystal superalloy for different solutioning cooling rates. Mater Sci Eng A 2014;601:145–52. https://doi.org/10.1016/j.msea.2014.02.046.

[13] Pierret S, Etter T, Evans A, Van Swygenhoven H. Origin of localized rafting in Ni-based single crystal turbine blades before service and its influence on the mechanical properties. Acta Mater 2013;61:1478–88. https://doi.org/10.1016/j.actamat.2012.11.024.

[14] Utada S, Rame J, Hamadi S, Delautre J, Mataveli Suave L, Villechaise P, et al. High-temperature pre-deformation and rejuvenation treatment on the microstructure and creep properties of Ni-based single crystal superalloys. In: Tin S, Hardy M, Clews J, Cormier J, Feng Q, Marcin J, et al., editors. Superalloys 2020, Springer International Publishing; 2020, p. 240–52. https://doi.org/10.1007/978-3-030-51834-9_23.

[15] Utada S, Rame J, Hamadi S, Delautre J, Villechaise P, Cormier J. Kinetics of creep damage accumulation induced by a room-temperature plastic deformation introduced during processing of AM1 Ni-based single crystal superalloy. Mater Sci Eng A 2020;789:139571. https://doi.org/10.1016/j.msea.2020.139571.

[16] Epishin A, Link T, Svetlov IL, Nolze G, Neumann RS, Lucas H. Mechanism of porosity growth during homogenisation in single crystal nickel-based superalloys. Int J Mater Res 2013;104:776–82.

https://doi.org/10.3139/146.110924.

[17] Epishin A, Link T. Mechanisms of high-temperature creep of nickel-based superalloys under low applied stresses. Philos Mag 2004;84:1979–2000. https://doi.org/10.1080/14786430410001663240.

[18] Steuer S, Villechaise P, Pollock TM, Cormier J. Benefits of high gradient solidification for creep and low cycle fatigue of AM1 single crystal superalloy. Mater Sci Eng A 2015;645:109–15. https://doi.org/10.1016/j.msea.2015.07.045.

[19] Cervellon A. Propriétés en fatigue à grand et très grand nombre de cycles et à haute température des superalliages base nickel monogranulaires. ISAE-ENSMA Ecole Nationale Supérieure de Mécanique et d'Aérotechique, 2018.

[20] Wright PK, Jain M, Cameron D. High Cycle Fatigue in a Single Crystal Superalloy: Time Dependence at Elevated Temperature. Superalloys 2004 (Tenth Int. Symp., TMS; 2004, p. 657–66. https://doi.org/10.7449/2004/Superalloys_2004_657_666.

[21] Epishin A, Link T, Nazmy M, Staubli M, Klingelhöffer H, Nolze G. Microstructural degradation of CMSX-4: Kinetics and effect on mechanical properties. Superalloys 20082, 2008, p. 725–31. https://doi.org/10.7449/2008/Superalloys_2008_725_731.

[22] Tinga T, Brekelmans WAM, Geers MGD. Directional coarsening in nickel-base superalloys and its effect on the mechanical properties. Comput Mater Sci 2009;47:471–81. https://doi.org/10.1016/j.commatsci.2009.09.013.

[23] Leidermark D, Moverare JJ, Johansson S, Simonsson K, Sjöström S. Tension/compression asymmetry of a single-crystal superalloy in virgin and degraded condition. Acta Mater 2010;58:4986–97. https://doi.org/10.1016/j.actamat.2010.05.032.

[24] Fedelich B, Epishin A, Link T, Klingelhöffer H, Künecke G, Portella PD. Experimental characterization and mechanical modeling of creep induced rafting in superalloys. Comput Mater Sci 2012;64:2–6. https://doi.org/10.1016/j.commatsci.2012.05.071.

[25] Leidermark D, Moverare JJ, Simonsson K, Sjöström S, Johansson S. Room temperature yield behaviour of a single-crystal nickel-base superalloy with tension/compression asymmetry. Comput Mater Sci 2009;47:366–72. https://doi.org/10.1016/j.commatsci.2009.08.012.

[26] Hermann W, Sockel HG, Han J, Bertram A. Elastic properties and determination of elastic constants of nickel-base superalloys by a free-free beam technique. In: Kissinger RD, Deye DJ, Anton DL, Cetel AD, Nathal M V., Pollock TM, et al., editors. Superalloys 1996, The Minerals, Metals, & Materials Society; 1996. https://doi.org/10.7449/1996/Superalloys_1996_229_238.

[27] Flouriot S, Forest S, Cailletaud G, Köster A, Rémy L, Burgardt B, et al. Strain localization at the crack tip in single crystal CT specimens under monotonous loading: 3D Finite Element analyses and application to nickel-base superalloys. Int J Fract 2003;124:43–77. https://doi.org/10.1023/B:FRAC.0000009300.70477.ba.

[28] Sabnis PA, Forest S, Cormier J. Microdamage modelling of crack initiation and propagation in FCC single crystals under complex loading conditions. Comput Methods Appl Mech Eng 2016;312:468–91. https://doi.org/10.1016/j.cma.2016.04.018.

[29] Busse C, Gustafsson D, Palmert F, Sjödin B, Almroth P, Moverare JJ, et al. Criteria evaluation for the

transition of cracking modes in a single-crystal nickel-base superalloy. Theor Appl Fract Mech 2020;106:102453. https://doi.org/10.1016/j.tafmec.2019.102453.

[30] Chen X, Sakaguchi M. Transition behavior from Mode I cracking to crystallographic cracking in a Ni-base single crystal superalloy. Int J Fatigue 2020;132:105400. https://doi.org/10.1016/j.ijfatigue.2019.105400.

[31] Suzuki S, Sakaguchi M, Inoue H. Temperature dependent fatigue crack propagation in a single crystal Ni-base superalloy affected by primary and secondary orientations. Mater Sci Eng A 2018;724:559–65. https://doi.org/10.1016/j.msea.2018.03.090.

[32] Neu RW. Crack paths in single-crystal Ni-base superalloys under isothermal and thermomechanical fatigue. Int J Fatigue 2019;123:268–78. https://doi.org/10.1016/j.ijfatigue.2019.02.022.

[33] Srivastava A, Gopagoni S, Needleman A, Seetharaman V, Staroselsky A, Banerjee R. Effect of specimen thickness on the creep response of a Ni-based single-crystal superalloy. Acta Mater 2012;60:5697–711. https://doi.org/10.1016/j.actamat.2012.06.043.

[34] Moverare JJ, Johansson S. Damage mechanisms of a high-Cr single crystal superalloy during thermomechanical fatigue. Mater Sci Eng A 2010;527:553–8. https://doi.org/10.1016/j.msea.2009.08.023.